remote sensing

MDPI

Article

Overestimated Fog-Top Entrainment in WRF Simulation Leading to Unrealistic Dissipation of Sea Fog: A Case Study

Li Zhang †, Hao Shi †, Shanhong Gao * and Shun Li

Key Laboratory of Physical Oceanography, College of Oceanic and Atmospheric Sciences, Ocean University of China, Qingdao 266100, China; zhangli2561@stu.ouc.edu.cn (L.Z.); shihao@stu.ouc.edu.cn (H.S.); lishun8561@stu.ouc.edu.cn (S.L.)

* Correspondence: gaosh@ouc.edu.cn

† These authors contributed equally to this work.

Abstract: Entrainment at the top of the planetary boundary layer (PBL) is of significant importance because it controls the upward growth of the PBL height. An option called ysu_topdown_pblmix, which provides a parameterization of fog-top entrainment, has been proposed for valley fog modeling and introduced into the YSU (Yonsei University) PBL scheme in the Weather Research and Forecasting (WRF) model. However, enabling this option in simulations of sea fog over the Yellow Sea typically results in unrealistic dissipation near the fog bottom and even within the entire fog layer. In this study, we theoretically examine the composition of the option ysu_topdown_pblmix, and then argue that one term in this option might be redundant for sea-fog modeling. The fog-top variables are employed in this term to determine the basic entrainment in the dry PBL, which is already parameterized by the surface variables in the original YSU PBL scheme. This term likely leads to an overestimation of the fog-top entrainment rate, so we refer to it as redundant. To explore the connection between the redundant term and unrealistic dissipation, a widespread sea-fog episode over the Yellow Sea is employed as a case study based on the WRF model. The simulation results clearly attribute the unrealistic dissipation to the extra entrainment rate that the redundant term induces. Fog-top entrainment is unexpectedly overestimated due to this extra entrainment rate, resulting in a significantly drier and warmer bias within the interior of sea fog. When sea fog develops and reaches a temperature lower than the sea surface, the sea surface functions as a warming source to heat the fog bottom jointly with the downward heat flux brought by the fog-top entrainment, leading the dissipation to initially occur near the fog bottom and then gradually expand upwards. We suggest a straightforward method to modify the option ysu_topdown_pblmix for sea-fog modeling that eliminates the redundant term. The improvement effect of this method was supported by the results of sensitivity tests. However, more sea-fog cases are required to validate the modification method.

Keywords: sea fog; fog-top entrainment; parameterization; overestimation; unrealistic dissipation

Citation: Zhang, L.; Shi, H.; Gao, S.; Li, S. Overestimated Fog-Top Entrainment in WRF Simulation Leading to Unrealistic Dissipation of Sea Fog: A Case Study. *Remote Sens.* **2024**, *16*, 1656. https://doi.org/10.3390/rs16101656

Academic Editor: Costas Varotsos

Received: 2 March 2024
Revised: 1 May 2024
Accepted: 3 May 2024
Published: 7 May 2024

1. Introduction

Sea fog is a hazardous weather phenomenon that occurs in the lower part of the atmosphere over the sea and coast [1]. It reduces atmospheric horizontal visibility to less than 1 km, and sometimes even lower, and has become a high-impact weather event comparable to tornadoes or, sometimes, even to hurricanes [2]. The Yellow Sea, depicted in Figure 1a, is a prominent maritime region in China known for its frequent occurrences of coastal and widespread sea fogs [1,3–5]. At times, a widespread sea fog may occupy almost half or more of the Yellow Sea (see a typical sea-fog episode illustrated in Figure 1b). Sea fog, which is distinguished by poor visibility, has significant impacts on a wide range of maritime activities, such as maritime transportation, marine fishing and aquaculture, and large-scale offshore activities, resulting in serious consequences. Furthermore, the presence of high humidity in sea fog can lead to an increase in atmospheric turbidity in

coastal regions, which can have a negative impact on the effectiveness of harnessing solar energy at sea [6].

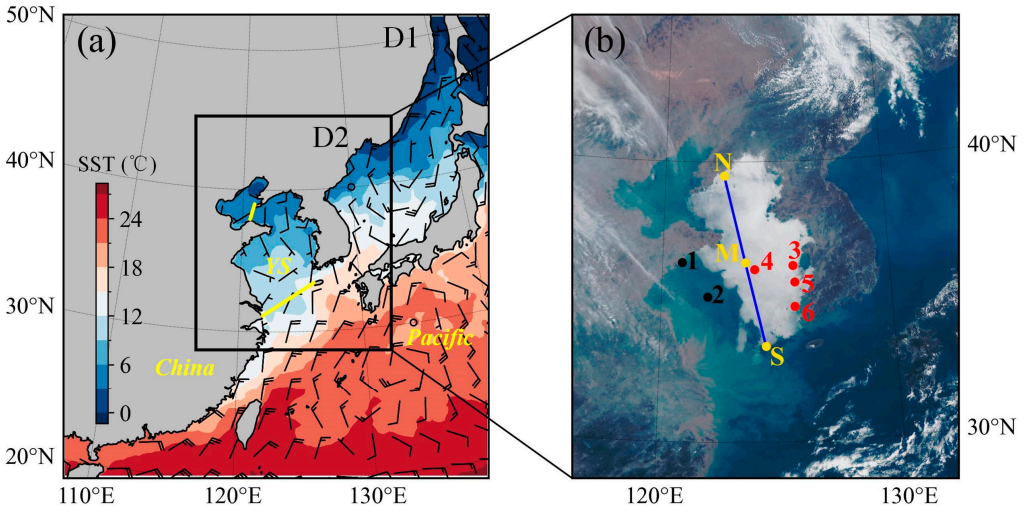

Figure 1. (**a**) Geographic map of the Yellow Sea (YS, the region bounded by two yellow lines) and two nesting domains (D1 and D2) used for WRF simulations; and (**b**) snapshot of Himawari-8 visible-light cloud imagery at 1330 local standard time (LST; LST = UTC + 8 h on 25 March 2021 derived from Japan Meteorological Agency website. Distributions of sea-surface temperature (SST, color-shaded) (The SST data is provided daily from North-East Asian Regional Global Ocean Observing System (NEAR-GOOS) dataset) and 10-m wind field (barbs; a full barb denotes 4 m s^{-1}) (The 10-m wind data is provided hourly from The European Centre for Medium-Range Weather Forecasts reanalysis 5 (ERA5; 0.25° × 0.25° horizontal resolution)) at 1100 LST on 25 March 2021 are shown in panel (**a**). Panel (**b**) depicts the orbital track of Cloud-Aerosol Lidar and Infrared Pathfinder Satellite Observations (CALIPSO) over the sea-fog area as a blue line with makers N, M and S for later analysis in Section 3.1, while six buoy sites are presented by solid black and red dots.

Numerical simulation has become as a primary approach to investigating and forecasting sea fog. Due to its high sensitivity to initial conditions, data assimilation is critical for the accurate numerical simulation of sea fog [7–11]. Due to the fact that sea fog is a cloud process occurring within the atmospheric boundary layer (also known as the planet boundary layer, PBL), relying solely on data assimilation does not guarantee accurate sea-fog forecasts when the numerical weather model employed is defective, particularly with regard to the PBL and microphysics schemes. These two schemes significantly influence the efficacy of sea-fog simulation. Prior research has shown that, when modeling sea fog with the Weather Research and Forecasting (WRF) model [12,13], the combination of the YSU (Yonsei University) PBL scheme [14] (hereafter YSU scheme) and the Perdue–Lin microphysics scheme [15,16] (hereafter Lin scheme) yields much better outcomes compared to other combinations [17]. As far as we know, the YSU scheme is currently the most popular and widely used PBL scheme for conducting numerical studies on sea fog using the WRF model [9,18–20]. Even so, evaluations of, and improvements to, the YSU scheme have been continuously progressing for fog simulation [18,21,22].

The turbulence process described in the PBL scheme plays a crucial role in the formation and development of sea fog. Most sea fogs over the Yellow Sea are categorized as advection cooling fogs [1,3,4]. Warm and humid air masses, which originate from a warm sea region and are already well-mixed, are transported to the cooler sea surface of the Yellow Sea by a favorable weather system with southerly winds. This causes the air to cool down and condense through turbulent mixing. Based on previous studies [3,19,23–29], Figure 2 schematically shows the evolution of typical advection cooling sea fog. During the initial generation phase, turbulence generated by vertical wind shear near the sea surface is critical in spreading cooling from the colder sea surface upwards (see "bottom-up diffusion"

in Figure 2), promoting sea-fog formation [3,24]. As the sea fog grows up to a certain depth, several physical processes at the fog top become important, including longwave radiative cooling, entrainment, and evaporation. The fog top can be regarded as an interface bridging the fog and the clear sky. The sea fog below is more humid, colder, and contains many fog droplets, quantified as liquid water content (LWC), whereas the clear sky above is less humid and warmer. Thus, longwave radiative cooling (LRC) at the fog top becomes effective in this situation. Consequently, a positive feedback process appears at the interface involving LWC and longwave radiative cooling (hereafter termed "LWC-LRC feedback"). In other words, longwave radiative cooling stimulates an increase in LWC, and in turn, the increased LWC boosts longwave radiative cooling. The positive feedback process makes the fog top another "cold surface" opposite to the colder sea surface and hence produces a peak value of LWC near the top of the fog layer (hereafter termed "fog-top LWC peak"). This is supported by previous numerical modeling with fine vertical resolution [3,19,30]. In particular, a large eddy simulation has revealed it in detail and identifies it as the result of longwave radiative cooling at the fog top [30].

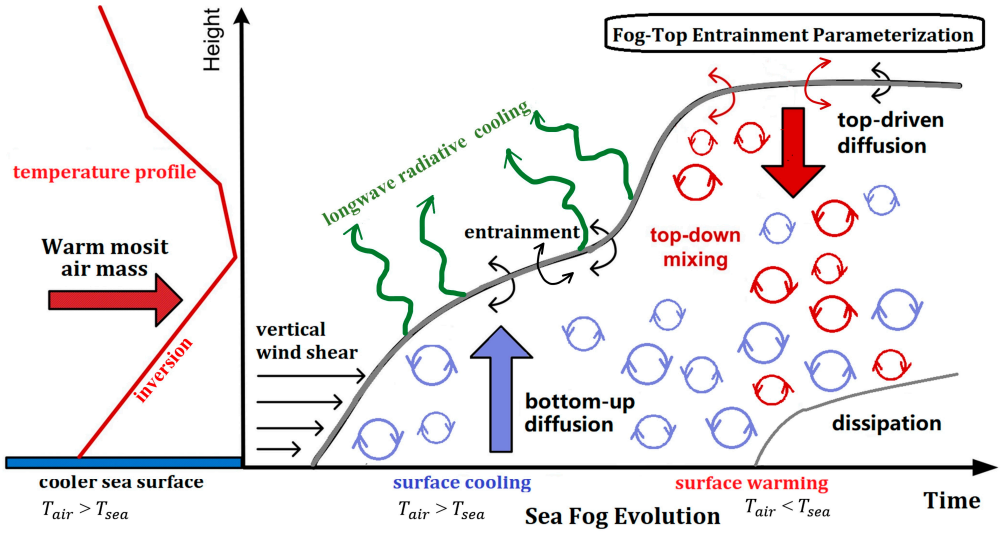

Figure 2. Schematic diagram of sea-fog evolution indicating the inversion before sea-fog formation, bottom-up diffusion generated by vertical wind shear, top-driven diffusion induced by fog-top cooling, and top-down mixing by fog-top entrainment and cooling. The arrow on the left shows warm-moist advection, the upward and downward arrows mark the sources and transport directions of turbulence, the curls mean turbulent eddies (red and blue circles represent the chaotic turbulent eddies driven by top-driven diffusion and bottom-up diffusion, respectively), and the bold and thin gray curves denote the fog top and fog bottom, respectively. T_{air} and T_{sea} denote 2-m air temperature and sea-surface temperature, respectively. See more details in the text. This figure is derived from Figure 2 in the paper by Yang and Gao [19].

Besides the feedback process associated with LWC and longwave radiative cooling on the fog top, there is also another important feedback process. The longwave radiative cooling can intensify the entrainment (see "top-driven diffusion" in Figure 2), and the negatively buoyant downdrafts formed from the entrained air produce additional turbulence that can enhance entrainment and mixing (see "top-down mixing" in Figure 2). The newly entrained air can then also become unstable and sink, leading to even more turbulence and more entrainment. This positive feedback process (hereafter termed "entrainment–mixing feedback") can cause the sea fog to entrain large amounts of dry air, resulting in the evaporation and even dissipation of the fog [23]. Therefore, it can be stated that the fog-top entrainment parameterization is an important issue in sea-fog modeling.

Starting from version 3.7, the WRF model includes the updated YSU scheme with an additional option called ysu_topdown_pblmix based on the work by Wilson and Fovell [21].

They suggested this approach to address the challenge of predicting valley radiation fog due to the absence of the physics required to lift fog into a low stratus. The option ysu_topdown_pblmix introduces an additional entrainment term to account for the turbulence generated by cloud-top (radiative and evaporative). Yang and Gao [19] explored the impact of this additional option on sea-fog modeling in a case over the Yellow Sea. They reported that enhanced buoyant turbulence causes warming and dehumidifying, which slightly lifts the sea-fog bottom and substantially reduces unrealistic fog area predictions. As a result, we activated this option in the WRF-based Yellow Sea fog prediction system we developed. However, we noticed that the bottom of the sea fog lifts unexpectedly in many forecasting results. This side effect of the option ysu_topdown_pblmix was confirmed by Tian et al. [31]. They stressed the necessity of activating the option ysu_topdown_pblmix for numerical simulations of fog in the North China Plain, but also pointed out that the higher entrainment rate leads to faster lifting of the fog layer and quicker dissipation of the low-level fog.

We conjecture that the unrealistic dissipation at the bottom of the sea fog is triggered by overestimated entrainment. The purpose of this study is to investigate the fog-top entrainment parameterization described in the option ysu_topdown_pblmix, using a sea-fog case over the Yellow Sea. The remainder of the paper is organized as follows. Section 2 describes the methodology, which includes a brief overview of fog-top entrainment parameterization in the option ysu_topdown_pblmix, a budget contribution analysis of LWC and virtual potential temperature, and datasets. A typical sea-fog case, the model configuration, and the design of the numerical experiments are presented in Section 3. Section 4 shows the findings, investigating the correlation between overestimated entrainment and unrealistic dissipation, and proposes a modification for correcting the overestimation. Finally, conclusions and a discussion are provided in Section 5.

2. Methodology

2.1. Fog-Top Entrainment Parameterization

In the YSU scheme of the WRF model, the entrainment rate w_e, which drives the growth of the boundary layer, is determined by the average vertical heat flux of turbulence at the top of the boundary layer [32,33], denoted as $\overline{(w'\theta_v')_h}$. Thus, w_e is calculated by the following formula

$$w_e = -\frac{\overline{(w'\theta_v')_h}}{\Delta\theta_v}, \tag{1}$$

where $\Delta\theta_v$ represents the vertical difference of virtual potential temperature (θ_v) at the top of the boundary layer. When there is fog/stratus near the top of the boundary layer, $\overline{(w'\theta_v')_h}$ is formulated in two parts [21]: the first part is contributed by surface heat fluxes (hereinafter referred to as SHF_{mix}), while the second part results from the cooling effect of longwave radiation and the evaporation process at the fog top (hereinafter referred to as PBL_{mix}). The corresponding expression can be written as

$$\overline{(w'\theta_v')_h} = SHF_{mix} + PBL_{mix}. \tag{2}$$

Notice that the second term on the right side, PBL_{mix}, is the core of the option ysu_topdown_pblmix mentioned in the introduction.

The parameterization of the entrainment process at the PBL top originates with the cloudless boundary layer. The rate of entrainment in the boundary layer, under clear sky conditions, is predominantly governed by the underlying surface process. The two driving forces, mechanical shear and buoyant convection driven by ground heating, are widely used in the parameterization description of the entrainment process in many studies [32,34–36]. Based on these studies, in the original YSU scheme, Hong et al. [14] summarized the form of SHF_{mix} as

$$SHF_{mix} = -0.15\left(\frac{\theta_{vs}}{g}\right)\frac{w_m^3}{h}, \tag{3}$$

where θ_{vs} represents the virtual potential temperature at surface, h is the height of the boundary layer, g is the gravitational acceleration, and w_m is the velocity scale caused by surface layer turbulence. The coefficient of 0.15 is decided empirically using the results obtained from large eddy simulations [14]. Note that h is equivalent to the fog-top height when sea fog is present.

When fog is present in the boundary layer, the entrainment rate can be typically increased by 4–13 times compared to that in a dry boundary layer [33,36]. In their investigation of valley fog (radiation type), Wilson and Fovell [21] incorporated longwave radiative cooling and evaporative cooling mechanisms into the vertical heat flux at the fog top to improve the entrainment rate. They included these processes in the description of entrainment as follows:

$$PBL_{mix} = -A\left(\frac{\theta_{vh}}{g}\right)\frac{w_l^3}{h}, \tag{4}$$

$$A = 0.2(1 + \alpha_2 E). \tag{5}$$

In Equation (4), θ_{vh} represents θ_v at the top of boundary layer, w_l is the velocity scale at the top of the boundary layer produced by radiative cooling, A is an entrainment efficiency. As shown in Formula (5), A has a minimum value of 0.2 (i.e., a minimum threshold amplitude) to represent the entrainment efficiency in the dry convective boundary. The threshold of A is essential because A is the coefficient of the entire entrainment term in the previous studies [33,37]. In addition, E reflects the enhancement of the entrainment rate by the evaporation process with a corresponding coefficient α_2. The two significant fog-top processes, radiation and evaporation, are represented in w_l and E, respectively, in the following formulae

$$w_l^3 = \frac{gh}{\theta_h}\frac{I_h}{\rho_h c_p}, \tag{6}$$

$$E = \frac{L_v}{c_p}\frac{q_h}{\Pi\Delta\theta_v}. \tag{7}$$

In Formula (6), I_h, ρ_h, and θ_h are radiative flux divergence, air density, and potential temperature at the fog top, respectively, and c_p is the heat capacity at constant pressure for dry air. In Formula (7), L_v is the latent heat of vaporization, q_h is the liquid water and ice after mixing cross the inversion, and Π is the Exner function. Consequently, in the YSU scheme, the entrainment rate w_e can now be expressed as

$$w_e = \underbrace{0.15\left(\frac{\theta_v}{g}\right)\frac{w_m^3}{h\Delta\theta_v}}_{R1} + \underbrace{0.2\left(\frac{\theta_{vh}}{g}\right)\frac{w_l^3}{h\Delta\theta_v}}_{R2} + \underbrace{0.2 \times \alpha_2 E\left(\frac{\theta_{vh}}{g}\right)\frac{w_l^3}{h\Delta\theta_v}}_{R3}. \tag{8}$$

In the calculation of w_e in Formula (8), the term $R3$ should be the dominant term as it comprehensively considers the combined effects of radiative and evaporative cooling, which is the fundamental purpose of option ysu_topdown_pblmix. In the opinion of Wilson and Fovell [21], SHF_{mix} (i.e., the heat flux corresponding to the term $R1$) plays a minor role in the boundary layer with fog/stratus and can be neglected, so PBL_{mix} can be directly added to $\overline{(w'\theta_v')_h}$ to parameterize the entrainment process in the presence of fog/stratus. However, in a sea-fog episode, as the sea-fog layer develops over time, a cooler fog bottom and a relatively warmer sea surface cause the term $R1$ to become significantly effective. Furthermore, the term $R1$ should be used to estimate w_e for those areas where fog/stratus is absent, so that the term $R1$ should be retained to ensure consistency in the basic entrainment calculation throughout the simulation.

It is important to note that the reason why the term $R2$ appears in Formula (8) is because Formula (5) sets a minimum threshold amplitude of 0.2 for the dry boundary layer. However, the term $R1$ is already employed to parameterize fog-top entrainment by surface processes in the dry boundary layer. Inclusion of w_l in the term $R2$ leads to an additional entrainment rate considering radiative cooling in terms of actual effect.

Therefore, we deduce that the term $R2$ is redundant and designate it as a redundant term. The redundancy of the term $R2$ could cause an overestimation of the entrainment rate at the fog top, possibly resulting in unrealistic dissipation at the bottom of the sea fog.

2.2. Budget Contribution Analysis of LWC and θ_v

The LWC within sea fogs over the Yellow Sea is typically quantified using the cloud water mixing ratio (q_c), as demonstrated in previous studies [3,38]. Thus, the formation, development, and dissipation of sea fog can be regarded as a progression of q_c within the marine PBL. As a part of this study, analyzing the LWC budget contribution offers an exact method to look closely at the dissipation process at the bottom of the sea fog. As shown in previous studies [39–41], the q_c budget can be affected by specific physical processes. The contributions to the q_c budget in the WRF model can be described in a q_c tendency equation by

$$\frac{\partial q_c}{\partial t} = (q_c)_{adv} + \left(\frac{\partial q_c}{\partial t}\right)_{mp} + \left(\frac{\partial q_c}{\partial t}\right)_{dif}. \quad (9)$$

The terms on the right-hand side in Equation (9) correspond to the changes (i.e., decrease or increase) caused by advection (i.e., $\frac{\partial u_i q_c}{\partial x_i}$), microphysics, and turbulence diffusion, respectively. Specifically, the term 'microphysics' is mainly associated with processes such as condensation, evaporation, collision, and coalescence. On the other hand, the term 'turbulence diffusion' refers to the vertical transport by turbulence, as well as to the sedimentation of fog droplets and horizontal diffusion.

The LWC within sea fog can be affected by θ_v through the LWC-LRC feedback and the entrainment–mixing feedback. Similar to the budget contribution analysis of LWC, we also conducted an analogous examination for θ_v using the following equation

$$\frac{\partial \theta_v}{\partial t} = (\theta_v)_{adv} + \left(\frac{\partial \theta_v}{\partial t}\right)_{mp} + \left(\frac{\partial \theta_v}{\partial t}\right)_{dif} + \left(\frac{\partial \theta_v}{\partial t}\right)_{rad} + \left(\frac{\partial \theta_v}{\partial t}\right)_{aco}. \quad (10)$$

In Equation (10), the tendency of θ_v is governed by five terms on the right-hand side. These terms correspond to the changes of θ_v by advection, microphysics, turbulence diffusion, radiation, and acoustics, respectively. The first three terms are similar to the right-hand three terms in Equation (9), respectively. The fourth term relates to the radiation process, and the last term is relevant to acoustic waves, and is minor and can be omitted.

Because the WRF model cannot directly output the tendency of each term in Equations (9) and (10), we allowed the WRF model to output those variables corresponding to each term at a high frequency, such as every 3 min. In the calculation of a tendency, its differential was treated as a difference that was computed using two sequential outputs. The changes at 3 min of each term were taken to conduct budget analysis. To ensure that the calculation was correct, the values on both sides of the equation were examined to confirm their equivalence.

2.3. Data Sets

The eighth Himawari geostationary weather satellite (Himawari-8), operated by the Japan Meteorological Agency (JMA), provides infrared and visible cloud images with which to observe sea-fog scenarios. Himawari-8 satellite is a new-generation geostationary meteorological satellite from Japan that has been in use since 2015. It can provide high temporal resolution (per 10 min) and spatial resolution (e.g., 2 km) visible and near-infrared light observation data [42]. The Himawari-8 images used in this paper were obtained from the Central Weather Agency of the Ministry of Transportation of Taiwan province.

The CALIPSO (Cloud-Aerosol Lidar and Infrared Pathfinder Satellite Observation) satellite, which is equipped with the CALIOP (Cloud-Aerosol Lidar with Orthogonal Polarization) lidar. It has provided nearly continuous measurements of clouds and aerosols in the atmosphere since its launch on 28 April 2006 [43]. The vertical sample spacing of CALIPSO observation data can reach 30 m within an altitude of −0.5~8.2 km, which allows

for the observation and confirmation of the contour of vertical sea-fog profiles. This is achieved by analyzing the overall attenuation backscatter coefficient at a wavelength of 532 nm (β'_{532nm}). When β'_{532nm} is greater than 0.03 $km^{-1}sr^{-1}$ in two consecutive layers or more, it is judged as fog [44]. It is important to mention that the threshold of 0.03 may be slightly higher, but this can enhance the reliability of fog verification. When the fog exists, the fog-bottom and fog-top are judged with the criterion of $\beta'_{532nm} > 0.03$ $km^{-1}sr^{-1}$ from bottom to top based on the data above the surface. If the first layer above the surface is foggy, the fog-bottom height is specified as 0 m. A seven-point moving average is used with the fog-top and fog-bottom height to mitigate drastic fluctuations. Additionally, fog dissipation is assessed through buoy measurements obtained from the International Comprehensive Ocean-Atmosphere Data Set (ICOADS).

The European Centre for Medium-Range Weather Forecasts reanalysis 5 (ERA5; 0.25° × 0.25° horizontal resolution and three-hourly interval) [45] is employed to drive the WRF simulation. The sea-surface temperature (SST) from the North East Asian Regional Global Ocean Observing System (NEAR-GOOS; 0.25° × 0.25°, daily) provides the ocean conditions for the WRF simulation.

3. Numerical Experiments

3.1. Sea-Fog Case

A widespread sea-fog event occurred over the Yellow Sea during 24–25 March 2021. Figure 3 depicts the satellite-observed cloud images of the sea-fog development process. It became apparent that the sea fog originated in the northern region of the Yellow Sea on the night of March 24 (Figure 3a) and subsequently expanded towards the south (Figure 3b–d). Starting at 0800 LST (local standard time; LST = UTC + 8 h) on March 25 (Figure 3e), it appears that the sea fog reached the mature phase, and the portion on land rapidly dispersed after sunrise (cf. Figure 3e,f). Nevertheless, its portion over the sea exhibited a gradual rate of progress (Figure 3e–g). The western boundary of sea fog over the central region of the Yellow Sea was slowly expanding westward, as shown in Figure 3f,g. The sea fog persisted until at least the evening (Figure 3h).

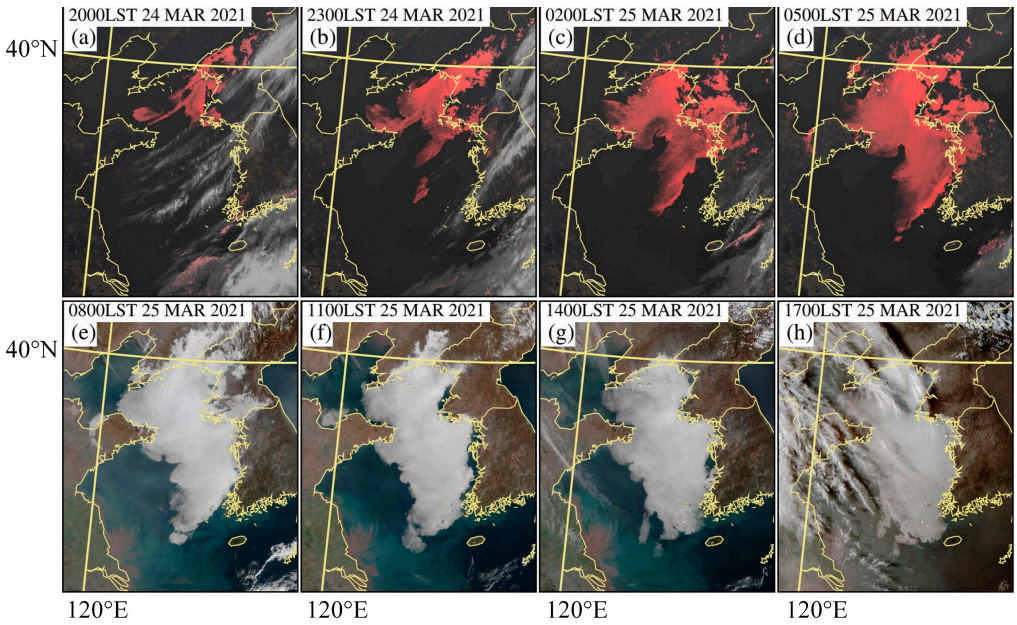

Figure 3. Sea-fog scenarios observed by Himawari-8 satellite. The red-color shaded patches in panels (**a**–**d**) denote nighttime fog, while the visible cloud images in panels (**e**–**h**) are used for daytime fog.

Based on previous research [10,46], the brightness of a sea-fog patch in a visible cloud image can be used to estimate the depth of sea fog, with a brighter color indicating a higher fog top. Observing the fog patch shown in Figure 3e–g, the eastern portion of the sea fog

appears to be brighter white than the western portion. As a result, the fog tops are higher in the east and lower in the west (hereafter termed "higher-E and lower-W"). Figure 4 clearly illustrates this higher-E and lower-W feature, showing the visible albedo averaged from the Himawari-8 satellite data at three visible bands (i.e., 0.45 μm, 0.51 μm, and 0.86 μm).

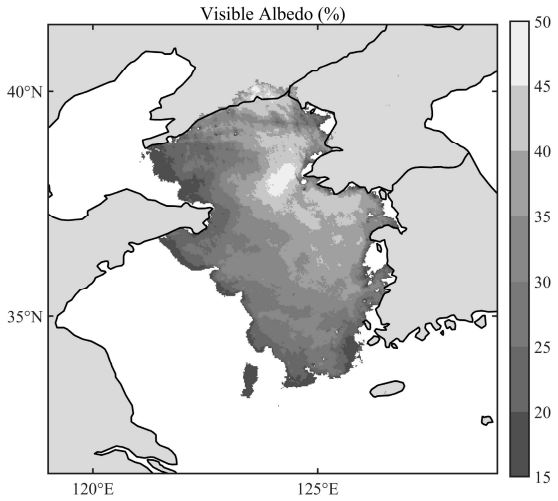

Figure 4. Visible albedo derived from the Himawari-8 satellite at 1330 LST on 25 March 2021. The feature of "higher-E and lower-W" is evident.

The CALIPSO satellite crossed over the sea fog at around 1336 LST on March 25. The blue line N-S in Figure 1b represents the path of the CALIPSO satellite as it crossed over the sea fog, and Figure 5 displays the corresponding intersection of the total 532-nm attenuated backscatter signals (i.e., aforementioned β'_{532nm}) of the CALIPSO. The threshold of 0.03 specified in Section 2.3 is used to distinguish sea fog in Figure 5, where the top and bottom heights of the fog are represented by red lines. As shown in Figure 5, the sea fog top fluctuates above 140 m in many locations, occasionally reaching or exceeding 200 m. In the area just southeast of location N, the top of the sea fog with a dissipated bottom reaches around 200 m. In contrast, the bottom does not dissipate in other regions, especially near location S.

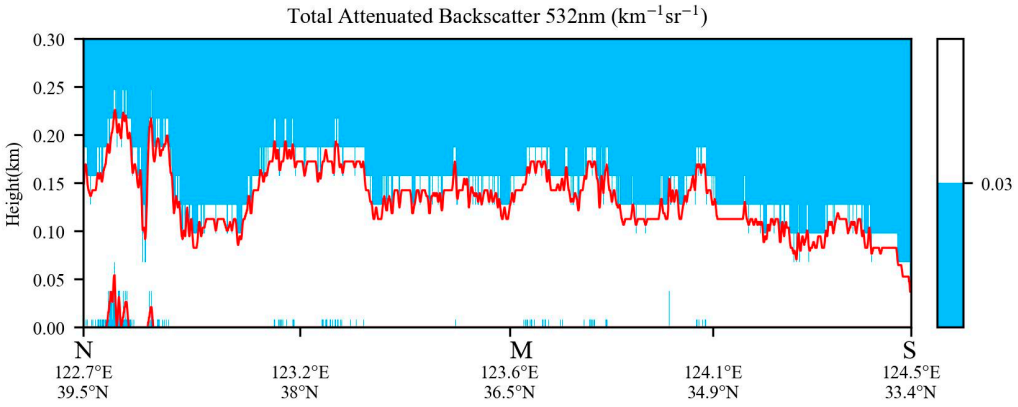

Figure 5. Representation of sea fog (black-gray-white shade) diagnosed from the total 532-nm attenuated backscatter signals of the CALIPSO data along the orbital track N-S in Figure 1b around 1300 LST on 25 March 2021. The red lines denote the top and bottom of the sea fog.

From the analysis on β'_{532nm} of CALIPSO, it appears that the southern portion of the fog bottom did not dissipate around 1300 LST on 25 March. Also, six buoys provided hourly measurements of sea-surface temperature (SST) and 2-m air temperature (see Figure 1b for the buoy sites as black and red solid dots). Unfortunately, humidity-related variables are not available. Previous studies on the sea fog over the coastal waters of China reveal that

the 2 m air temperature within the sea fog is frequently observed or simulated as lower than SST [26,47,48]. Figure 6 displays a time series of hourly differences between the 2 m air temperature and SST ($T_{\mathrm{air-sea}}$) at six buoys (see Figure 1b for their locations). Buoys 1 and 2 are situated in a clear-sky region, while buoys 3–6 are situated within the fog (Figure 1b). In Figure 6, buoys 3–6 consistently had $T_{\mathrm{air-sea}}$ values below 1 °C, especially after 1100 LST. These values were significantly lower than those observed at nearly the same latitude (buoys 1 and 2) and continue to fall, eventually falling below 0 °C. The continual decline in $T_{\mathrm{air-sea}}$ could be due to the development of sea fog or cold advection. The region covering buoys 3, 5, and 6 experienced prevailing southerly winds originating from the warmer sea area (see winds and SSTs in Figure 1a), indicating that there was no occurrence of cold advection. Therefore, there is a strong likelihood that fog remained in this region.

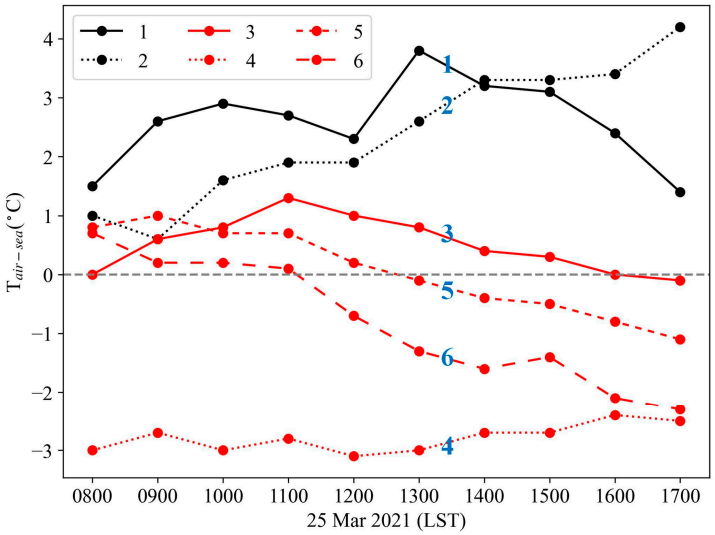

Figure 6. Time series of hourly differences between 2 m air temperature and SST ($T_{\mathrm{air-sea}}$) at six buoys during the period from 0800 LST to 1700 LST on 25 March 2021.

The analysis above demonstrates the development of sea fog, with a particular focus on its height. It also underlines the absence of fog-bottom dissipation in the southern foggy region after 1300 LST. These findings serve as crucial benchmarks for assessing the effectiveness of the next numerical experiments.

3.2. Model Configuration

The Advanced Research Core of the WRF model, version 4.3 (ARW) [13], was employed to simulate the sea fog scenario described earlier. Figure 1a shows the simulation's two one-way nested domains. The two domains have horizontal resolutions of 30 and 10 km, respectively. The vertical coordinates of the model are composed of 57 full-η vertical levels (Full-η levels: 1.0000, 0.9975, 0.9935, 0.9899, 0.9861, 0.9821, 0.9777, 0.9731, 0.9682, 0.9629, 0.9573, 0.9513, 0.9450, 0.9382, 0.9312, 0.9240, 0.9165, 0.9088, 0.9008, 0.8925, 0.8835, 0.8730, 0.8580, 0.8380, 0.8160, 0.7918, 0.7625, 0.7084, 0.6573, 0.6090, 0.5634, 0.5204, 0.4798, 0.4415, 0.4055, 0.3716, 0.3397, 0.3097, 0.2815, 0.2551, 0.2303, 0.2071, 0.1854, 0.1651, 0.1461, 0.1284, 0.1118, 0.0965, 0.0822, 0.0689, 0.0566, 0.0452, 0.0346, 0.0249, 0.0159, 0.0076, and 0.0000) up to 50 hPa, with 21 full-η levels located within the lowest 1 km.

The YSU PBL scheme [14] with the ysu_topdown_pblmix option [21], was used in conjunction with the revised MM5 (Fifth-generation Mesoscale Model) surface layer scheme [49]. The chosen physical options for the simulations consisted of the Lin microphysics scheme [15], the rapid radiative transfer model for general circulation model shortwave and longwave radiation schemes [50], the Kain–Fritsch cumulus scheme [51], and the unified Noah land surface model [52]. To improve accuracy in modeling the quantity of liquid water in fog, it is necessary to consider the gravitational settling of fog

droplets. This has been discussed in studies such as those by Bergot et al. [53] and Zhou and Ferrier [54]. The simulations were performed by configuring the grav_settling option to 2.

3.3. Experimental Design

Four numerical experiments were designed and subsequently carried out to investigate the option ysu_topdown_pblmix. These experiments, as outlined in Table 1, served the purpose of investigating specific aspects. Two experiments, Exp-orig and Exp-notpd, were conducted to investigate the influence of fog-top entrainment on the simulation of sea fog. The ysu_topdown_pblmix option was enabled in one experiment but disabled in the other. As stated in Section 2.1, since the term $R1$ cannot be neglected, the term $R2$ in the entrainment-rate calculation is probably redundant, whereas the term $R3$ is essential. Two additional experiments, Exp-noR1 and Exp-noR2, were performed to investigate the functions of the terms $R1$ and $R2$ (as described in Formula (8)) in the process of fog-top entrainment.

Table 1. List of the numerical experiments.

Experiments	Specification	Purpose
Exp-orig	Run with the ysu_topdown_pblmix option enabled	Assess the necessity of ysu_topdown_pblmix option
Exp-notpd	Run with the ysu_topdown_pblmix option disabled	
Exp-noR1	As in Exp-orig, but the term $R1$ is removed	Investigate the function of $R1$
Exp-noR2	As in Exp-orig, but the term $R2$ is removed	Investigate the function of $R2$

In all experiments, the WRF model was driven by initial and lateral boundary conditions extracted from the ERA5 datasets, incorporating the SST data of NEAR-GOOS. The WRF model ran, starting at 0800 LST on 24 March 2021, for a duration of 36 h. The model was integrated at fixed time steps of 180 s and 60 s for domains D1 and D2, respectively. The initial 12 h period was dedicated to the process of spin-up, while the subsequent 24 h period was allocated for a thorough examination of the experimental results. The diagnostics were carried out on the inner domain D2 (Figure 1a), and the WRF model output was stored in two products at intervals of every half-hour and three minutes, respectively. The 3-minute product was specifically designed for performing the budget analysis of LWC and θ_v.

To determine the area and height of simulated sea fog based on the WRF model output, a threshold of 0.016 g kg^{-1} for liquid water content (LWC) was utilized, as suggested by previous studies [10,18,19,55,56].

4. Results

4.1. Assessment of Simulated Sea Fog

The primary focus of the simulation results for sea fog was the fog area. Because it is challenging to accurately determine the extent of sea fog over the Yellow Sea based only on a small number of observations from ships and buoys, satellite visible and infrared images are commonly used as reliable evidence of sea fog (hereafter termed "observed sea fog"). Figure 3 depicts the observed sea fog that is distinguished from Himawari-8. Nevertheless, this kind of observed sea fog is more properly referred to as fog or stratus. To ensure a fair comparison between the simulated and observed sea fog, we used a bird's-eye view to determine the simulated sea fog. The simulated sea fog was defined as areas where the following criteria were met: the LWC, denoted as the variable q_c, at the lowest model level is greater than 0.016 g kg^{-1}, or the cloud-top height of the stratus is lower than 400 m [56]. The cloud-top was diagnosed by observing the LWC at model levels from bottom to top and identifying the point where it abruptly falls below 0.016 g kg^{-1}. The criterion of

0.016 g kg^{-1} corresponds to a visibility of less than 1 km, as calculated using the visibility formula by Stoelinga and Warner [57]; advection sea fogs are deeper than other types of fog but rarely exceed 400 m [56]. Figure 7 displays the simulated sea fog, including its areas and heights, for all experiments conducted between 0800 LST and 1700 LST on March 25.

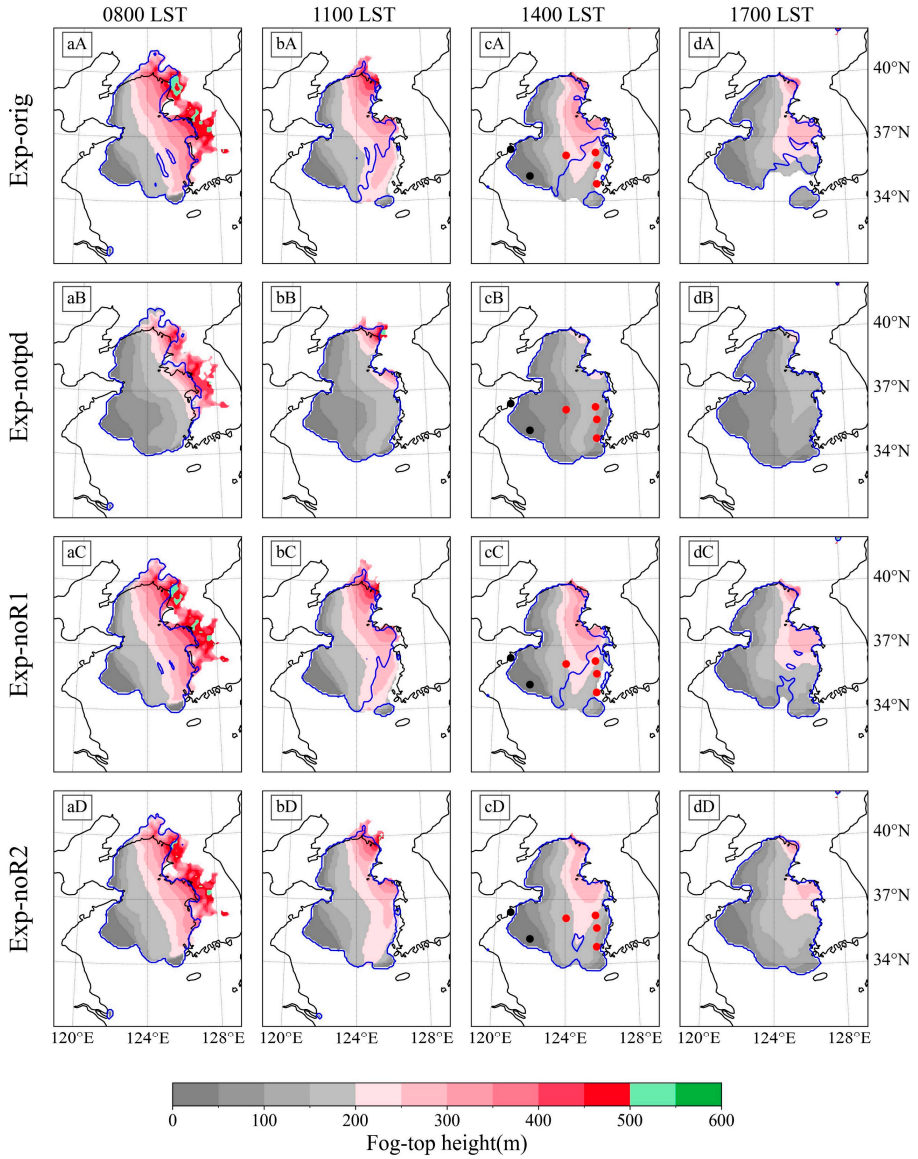

Figure 7. Spatial distributions of simulated sea fog from: (**aA**–**dA**) Exp-orig; (**aB**–**dB**) Exp-notpd; (**aC**–**dC**) Exp-noR1; and (**aD**–**dD**) Exp-noR2. The color-shaded region denotes sea-fog depth, and the blue contour depicts the sea-fog area at 10-m height above sea level with a value of LWC greater than 0.016 g kg^{-1}. The solid dots in panels at 1400 LST denote the buoy sites shown in Figure 1b. The rows correspond to the four experiments and the columns represent four different time points, which are annotated at the top and left sides of the figure.

All experiments, except for Exp-orig, essentially reproduce the features of sea-fog development during the daytime. This is seen by comparing the simulated sea-fog coverage with the observed sea-fog coverage in Figure 3. However, Exp-orig shows a noticeable dissipation around 1700 LST in the southern region, as shown in Figure 7dA. Upon closer inspection, significant differences can be seen in fog-top height (color shades) and fog area (blue contours). Note that the areas where the blue contours do not overlap with the color shades signify dissipation (as shown in Figure 7cA). Regarding sea-fog dissipation, the four experiments can be grouped as follows: Exp-notpd and Exp-noR2 exhibit no dissipation,

whereas Exp-orig and Exp-noR1 exhibit dissipation. As for fog-top height, Exp-notpd has a significantly lower height compared to the other experiments, and the feature of "higher-E and lower-W", observed by the Himawari-8 satellite (Figure 4) and discussed in Section 3.1, is not as well-captured as the other experiments.

Additional analysis was performed to gain insights of both fog-top height and the vertical structure of the simulated liquid water content. Figure 8 displays the vertical cross-section of LWC (i.e., q_c) for the four experiments along the north–south orbital track of CALIPSO shown in Figure 1b. The LWC within fog is significantly higher in Exp-notpd than in other experiments, with its maximum value shifted downwards to even reach the middle of the fog layer. This is not consistent with the "fog-top LWC peak" feature mentioned in Section 1, whereas the "fog-top LWC peak" feature appears to be reasonable in the other experiments. However, the average fog-top heights of both Exp-orig and Exp-noR1 appear to have a bias towards being higher, and unrealistic dissipation at the bottom of sea fog is clearly evident (Figure 8a,c).

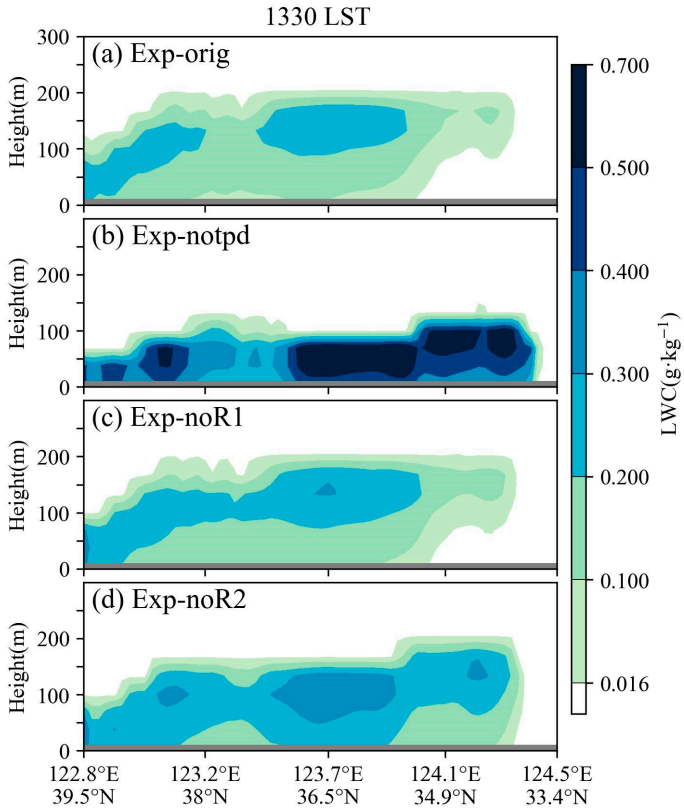

Figure 8. Vertical structure of the simulated liquid water content along the north–south orbital track of CALIPSO, indicated by the line N-S in Figure 1b.

After comparing the simulated sea fog with the observed facts, an assessment was conducted to evaluate the performance of the four experiments. The assessment focused on the following four examination items:

- Is the feature of "higher-E and lower-W" well captured?;
- Is the feature "fog-top LWC peak" evident?;
- Are the fog top heights appropriate?;
- Is the absence of unrealistic dissipation true?

Table 2 shows the assessment results. Comprehensively considering all four examination items, Exp-noR2 demonstrates the best result compared to the other experiments. Exp-notpd performs the worst, whereas Exp-noR1 and Exp-orig perform similarly. It can be inferred that disabling the option ysu_topdown_pblmix has a substantial adverse impact, resulting in a fault that hinders the vertical development of sea fog, as demonstrated in

Exp-notpd. Although enabling the option ysu_topdown_pblmix can effectively fix this fault, which has been pointed out by Yang and Gao [19], it has a side effect that causes sea fog to dissipate, starting from the bottom and then throughout the entire fog layer (cf. Figure 7cA,dA). It can be roughly confirmed that the unrealistic dissipation is closely related to the redundancy of the term $R2$ in the option ysu_topdown_pblmix, which introduces an extra entrainment rate at the fog top and could lead to the unrealistic dissipation.

Table 2. Summary of the assessment of all experiments. A mark of $\surd$ or $\times$ indicates that the answer to the corresponding examination item in the text is yes or no, respectively. The experiment with more points (i.e., $\surd$) performs better.

Experiments	Examination Items				Activation Status of ysu_topdown_pblmix
	Higher-E and Lower-W	Fog-Top LWC Peak	Fog-Top Heights	Absence of Dissipation	
Exp-orig	$\surd$	$\surd$	$\times$	$\times$	On
Exp-notpd	$\times$	$\times$	$\times$	$\surd$	Off
Exp-noR1	$\surd$	$\surd$	$\times$	$\times$	On without $R1$
Exp-noR2	$\surd$	$\surd$	$\surd$	$\surd$	On without $R2$

We performed an additional experiment, labeled Exp-noR3, in which the term $R3$ was excluded. Compared with the results of the other experiments illustrated in Figures 7 and 8, the outcome of Exp-noR3 (omitting figures) closely resembles that of Exp-notpd for the simulated area. However, when comparing its simulated sea-fog top to the "higher-E and lower-W" feature observed in Figure 4, Exp-noR3 is not as satisfactory as Exp-noR2. Regarding the vertical structure of LWC, the "fog-top LWC peak" characteristic in Exp-noR3 is inferior to that of Exp-noR2. Hence, it demonstrates that the redundant term is $R2$, not $R3$.

4.2. Explanation for Unrealistic Dissipation

An investigation was carried out to examine the relationship between fog-top entrainment and unrealistic dissipation at the bottom of the fog in the experiments Exp-orig and Exp-noR1. The investigation focused on the southern part of the N-S vertical cross-section, specifically the M-S section shown in Figures 1b and 5, where the unrealistic dissipation occurred. Figure 9 shows the evolutions of the fog top and LWC within the fog over time, with a specific focus on the dissipation of fog at the bottom (where $q_c < 0.016$ g kg^{-1}). The figure also includes information about the entrainment rate (w_e) and its three components ($R1$, $R2$, and $R3$; defined in Formula (8)), as well as the tendencies of θ_v generated by turbulent diffusion and longwave radiation (see Equation (10)).

Figure 9 shows that the fog top gradually rose with time after 0900 LST (Figure 9bA), while the LWC near the bottom, directly under the significantly increasing fog top, started to decrease (Figure 9bA,cA) and eventually dissipated (Figure 9dA–fA). The fog-top entrainment rate (w_e) appears to have increased considerably prior to the onset of fog-top growth, as indicated by the bold-dashed brown arrows crossing the first and second row of panels in Figure 9; the term $R1$ is the smallest of the three components of w_e, whereas the terms $R2$ and $R3$ are nearly equal and significantly larger (Figure 9aC–fC). Despite being the smallest component, the term $R1$ cannot be disregarded utterly. The term $R2$ has a significant impact on the overestimation of w_e, which in turn affects the simulation results for sea fog. It should be considered to modify the calculation of w_e; the actual improvement in simulation will be detailed in Section 4.3.

By observing the tendencies of θ_v, it is found that a cooling tendency at the fog top is apparent (Figure 9aD–fD), whereas a warming tendency at the fog bottom is significant (Figure 9aE–fE). According to the LWC-LRC feedback mentioned earlier in the introduction, cooling at the fog top is primarily dominated by the mechanism of longwave radiative cooling. The warming near the fog bottom, on the one hand, is partially influenced by the

warmer sea surface (Figure 9aE–fE). As the sea-fog layer gets thicker [25,26], the entire fog layer will cool, resulting in a cooler fog bottom and a relatively warmer sea surface (see "surface warming" in Figure 2) [19,26,58]. On the other hand, the warming within the entire fog layer is primarily due to entrainment–mixing feedback, because turbulent mixing controls a large portion of the warming. When comparing the vertical range and intensity of the fog-bottom warming produced by turbulent mixing (Figure 9aD–fD) and longwave radiation (Figure 9aE–fE), it is evident that the turbulent mixing had a considerably larger impact between 0830 LST and 1100 LST. For instance, especially around 1030 LST and 1100 LST, turbulent mixing caused a warming tendency of up to 6×10^{-4} K s^{-1} (about 2K h^{-1}) near the fog bottom (Figure 9eD,fD), accelerating dissipation near the fog bottom (Figure 9eA,fA). This illustrates the significant importance of the fog-top entrainment process in the dissipation of the fog bottom.

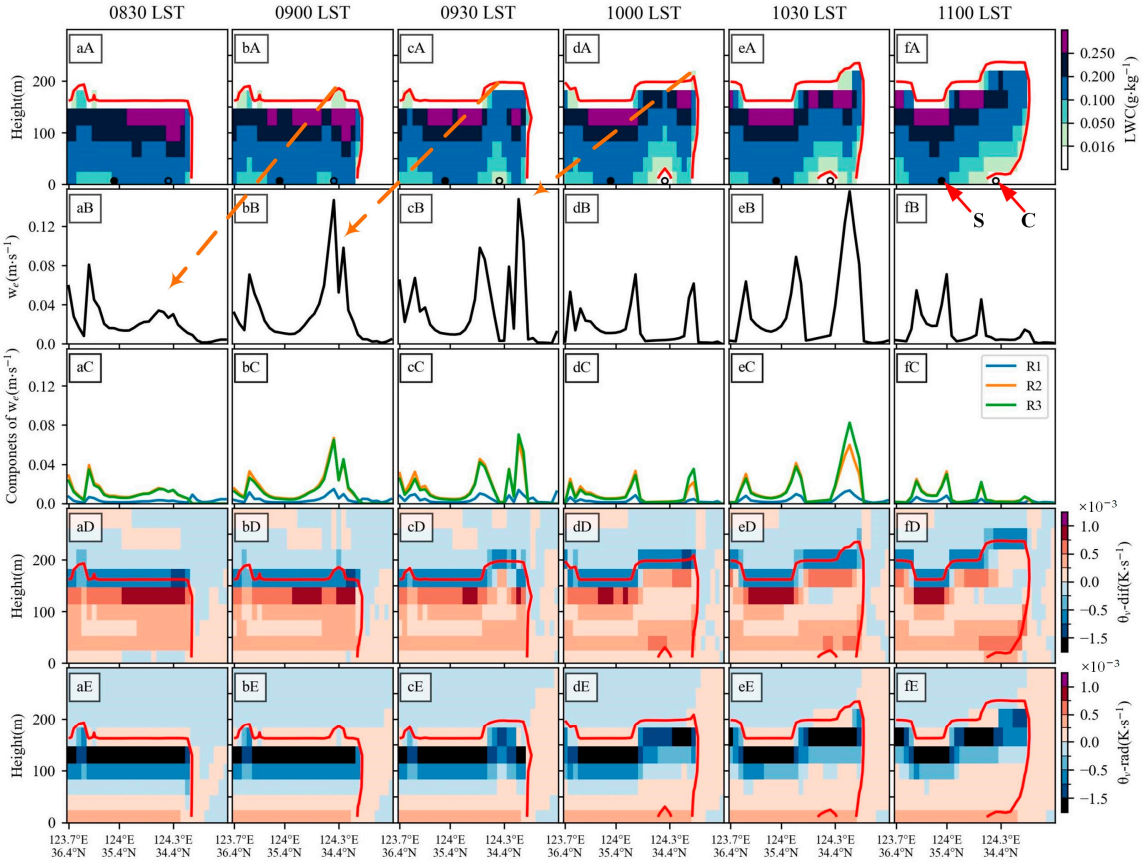

Figure 9. Evolution of the vertical structure of simulated sea fog with time for Exp-orig along the CALIPSO orbital track shown in Figure 5 during the period from 0830 LST to 1100 LST on 25 March 2021: (**aA–fA**) liquid water content (LWC, i.e., q_c); (**aB–fB**) w_e; (**aC–fC**) three components of w_e; (**aD–fD**) tendency of θ_v governed by turbulent mixing (θ_v-dif); and (**aE–fE**) tendency of θ_v governed by longwave radiation (θ_v-rad). Red lines denote LWC with a value of 0.016 g kg^{-1}, which outlines the sea fog/stratus. In the second row of panels, two dots, one solid and one circular, are labeled S and C, respectively. The bold-dashed brown arrows depict the relationship between the growth of fog-top and w_e. Further information may be found in the text.

In order to establish a clear link between the process of fog-top entrainment and fog-bottom dissipation, we investigated two specific positions at the bottom. The first position, marked as S in Figure 9, represents a scenario where unrealistic dissipation never took place. The second position, denoted as C in Figure 9, represents a scenario where unrealistic dissipation did occur. Figure 10 shows the temporal evolution of LWC and w_e over time, from 0830 LST to 1030 LST on 25 March. At around 0900 LST, the fog-top

entrainment at location C became considerably stronger, while the LWC at the fog bottom rapidly decreased until it approached zero at around 0950 LST (Figure 10a), indicating the dissipation of fog. However, the fog-top entrainment at location S remained very weak, and the LWC near the fog bottom also stayed around 0.12 g kg^{-1} (Figure 10b), indicating the maintenance of fog.

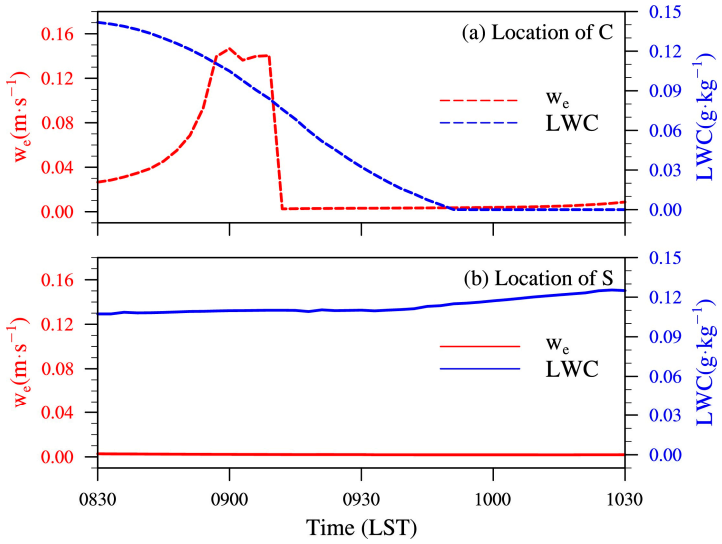

Figure 10. Temporal evolution of the LWC and w_e at (**a**) location C (dash lines); and (**b**) location S (solid lines) from 0830 LST to 1030 LST on 25 March 2021.

Subsequently, we conducted a thorough examination of each individual contribution to the q_c budget at the two designated locations, S and C, as depicted in Figure 9. The contributions to the q_c budget consist of the following three components: advection (adv); microphysics (mp); and turbulence diffusion (dif) (see more details in the description of Equation (9) in Section 2.2). For simplicity, these components are hereafter termed adv-term, mp-term, and dif-term, respectively. Figure 11a presents the analysis results, including the three components and q_c during the period from 0830 LST to 1100 LST on 25 March. The q_c budget term governed by turbulence diffusion is positive (i.e., term-dif; see green line), leading to an increase in fog droplets through turbulent transport. Conversely, the q_c budget term controlled by microphysics is negative (i.e., term-mp; see red line), resulting in a decrease in fog droplets by evaporation). The above two q_c budget terms nearly exhibit the evolution of a reversed-phase pattern, indicating that the evaporation process can nearly balance the increase in q_c caused by the turbulent transport process.

However, the balance between term-dif and term-mp is a local quasi-equilibrium. The q_c tendency, which governs the evolution of q_c with time, is dominated by this balancing and an additional term-adv. Normally, term-adv merely moves q_c from one part of the sea fog (where LWC is relatively more abundant) to another part (where LWC is relatively less abundant), and shares the same sign as the quasi-equilibrium result. At locations S and C from 0830 LST to 1000 LST (Figure 11a), it is observed that the local quasi-equilibrium result between term-dif and term-mp is positive at location S (i.e., term-mix plus term-mp; see black solid line) and negative at location C (see black dashed line). With the aid of the weak term-adv (see yellow solid line in Figure 11a) or the strong term-adv that has the same sign as that of term-mix plus term-mp (see yellow dashed line in Figure 11a), the positive q_c budget at location S and negative q_c budget at location C (see blue lines in Figure 11a) drive the evolution of q_c with time, as depicted in Figure 11b.

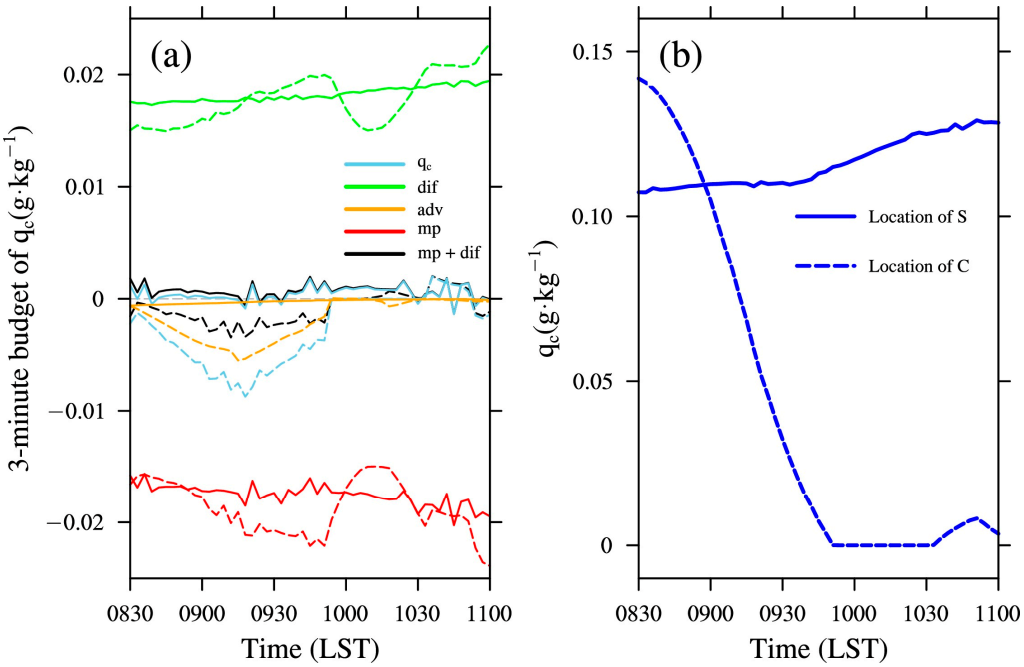

Figure 11. (**a**) Time series of the q_c budget at 3 min intervals for locations S and C (solid and dashed lines); and (**b**) of evolution of q_c. The period is from 0830 LST to 1100 LST on 25 March 2021. In panel (**a**), dif, adv, and mp, represent term-dif, term-adv, and term-mp in the text, respectively. The black line denoted by mp + dif represents the sum of term-mp and term-dif.

Therefore, we consider that the primary cause of the negative qc tendency resulting in unrealistic dissipation is the negative term-mp, indicating that the evaporation in microphysical processes surpasses the turbulent diffusion transport. The phenomenon is the result of the entrainment–mixing feedback occurring at the top of the sea fog, where the entrainment process brings drier and warmer air to the fog bottom, thereby enhancing the evaporation effect.

4.3. Modification of Fog-Top Entrainment

Compared with Exp-orig, unrealistic dissipation still occurs in Exp-noR1 with the removal of the term *R*1, but this unrealistic dissipation disappears in Exp-noR2 with the removal of the redundant term *R*2 (Figures 7 and 8). The analysis of the contributions to the q_c budget indicates that the entrainment–mixing feedback is important in dissipation at the bottom of sea fog. It is confirmed that unrealistic dissipation in the lower part of sea fog is attributed to additional entrainment introduced by the term *R*2. As mentioned earlier, the terms *R*2 and *R*3 are almost equal and significantly larger than the term *R*1. The terms *R*1 and *R*2 represent the impacts on the entrainment rate in the dry convective boundary layer. When fog is present within the boundary layer, the entrainment rate should be mostly dominated by the term *R*3. However, the sum of the terms *R*1 and *R*2 is greater than the term *R*3 (Figure 9aC–fC) in this simulation, inferring that the existence of the term *R*2 is inappropriate and leads to an overestimation of the entrainment rate. Moreover, this overestimation will increase with the increase in *R*3. Therefore, we proposed a modification of the option ysu_topdown_pblmix, namely, removing the term *R*2 in Formula (8).

We contrasted Exp-noR2 with Exp-orig to observe the increments caused by the term *R*2 to obtain a better understanding of its role in the simulation. Figure 12 illustrates the changes resulting from the removal of the term *R*2 (Exp-noR2 minus Exp-orig) within the M-S cross-section during the period from 0924 LST to 1000 LST, using the 3-minute product of the WRF simulations. It shows how the entrainment–mixing feedback affected the gradual formation of unrealistic dissipation near the fog bottom. Upon careful examination of the southern part of the M-S cross-section, it is clear that the rapid growth of the fog

top in Exp-orig was restrained. This can be observed by comparing the red solid line with the red dotted line (the first row of panels in Figure 12). Beneath the expanded fog top in Exp-orig, the LWC of Exp-noR2 was much higher than that of Exp-orig, with a difference of around 0.2–0.3 g kg^{-1}. The presence of the term *R*2 in Exp-orig caused the interior of the sea fog to become less humid through the entrainment–mixing feedback, resulting in the rapid dissipation of the fog bottom within approximately thirty minutes (from 0924 LST to 1000 LST). This can be seen by the circle dots and solid lines near the bottom of panels in Figure 12aA–dA, with the circle dots representing the same location as C in Figure 9). The removal of the term *R*2 from Exp-noR2 was beneficial because it corrected the drier bias that existed in Exp-orig (see the zone with a positive increment of LWC above the circle dot).

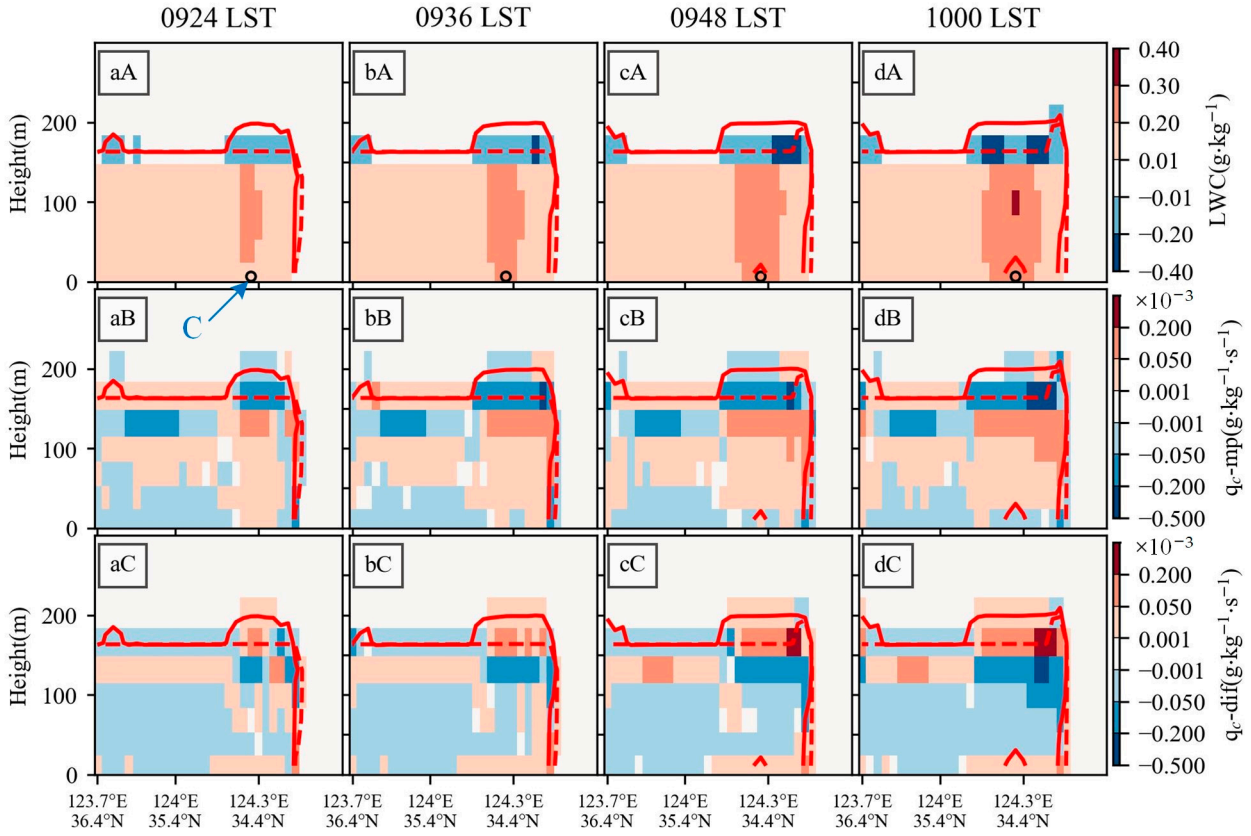

Figure 12. Distribution of Exp-noR2 minus Exp-orig along the CALIPSO orbital track shown in Figure 5 during the period from 0924 LST to 1000 LST on 25 March 2021 for the three variables: (**aA**–**dA**) liquid water content (LWC, i.e., q_c); (**aB**–**dB**) tendency of q_c governed by microphysics; and (**aC**–**dC**) tendency of q_c governed by turbulent mixing. The solid red line represents the fog-top height in Exp-orig, whereas the dashed red line represents it in Exp-noR2. The circle dot in the first row of panels is at the same position as location C in Figure 9.

Compared with Exp-orig, near the fog bottom, the evaporation effect in Exp-noR2 was weakened (see the zone of a negative increment in Figure 12aB–dB) and the increase in q_c caused by turbulent transport was enhanced (see the zone of a positive increment in Figure 12aC–dC). As a result, the dissipation did not occur in Exp-noR2. Since the quasi-equilibrium result of the evaporation in microphysics and turbulent transport near the fog bottom is closely related to the dissipation of sea fog, an analysis of the q_c budget at location C was conducted for both Exp-orig and Exp-noR2. Figure 13 shows the analysis result, demonstrating the time series of q_c budget and the evolution of q_c. From 0830 LST to 1000 LST, the results of Exp-noR2 were very similar to those of Exp-orig at Location S, where Exp-orig did not experience dissipation, but the sum of term-mp and term-dif was

larger and term-adv was significantly positive (cf. Figures 11 and 13). It is worth noting that the q_c budget of Exp-noR2 had a negative value between 1000 LST and 1100 LST (see solid light-blue line in Figure 13a). This led to an obvious decrease in q_c, but it still remained much higher than the fog criteria (i.e., 0.016 g kg^{-1}) (see solid line in Figure 13b).

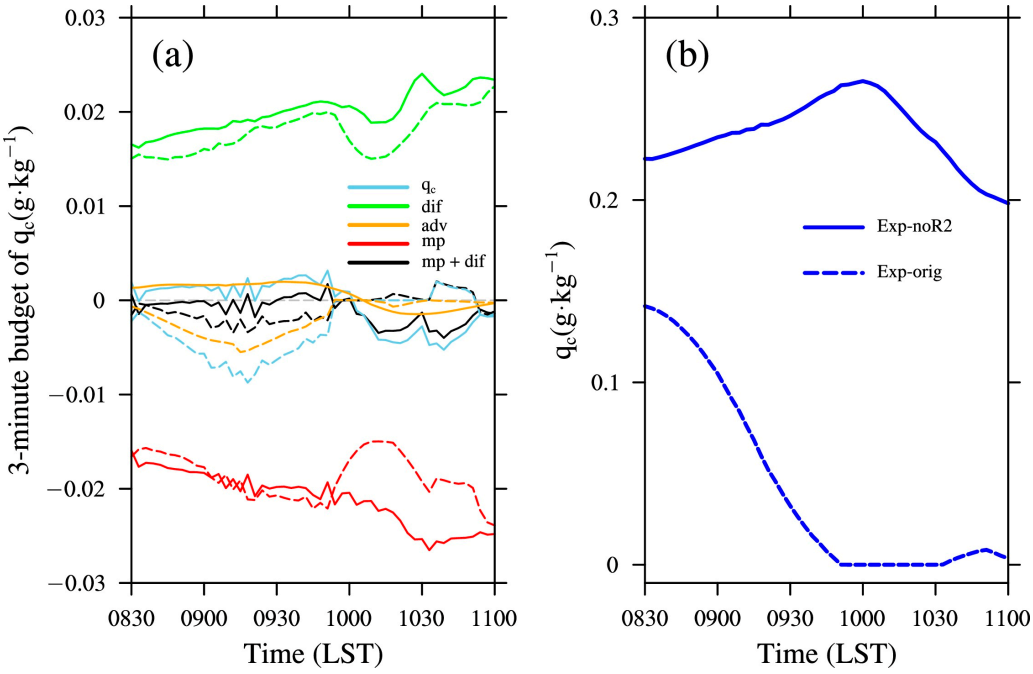

Figure 13. (**a**) Time series of the q_c budget at 3 min intervals for Exp-orig (solid lines) and Exp-noR2 (dashed lines); and (**b**) evolution of q_c. The period is from 0830 LST to 1100 LST on 25 March 2021. The definitions of dif, adv, mp, and mp+dif can be found in Figure 11.

We performed an evaluation of Exp-orig, Exp-noR1, and Exp-noR2 using the CALIPSO-observed heights of the fog top and fog bottom as the baseline, as depicted in Figure 5. As shown in Table 3, Exp-noR1 is slightly better than Exp-orig, while Exp-noR2 performs best and is closest to the observations. The improvement rates of Exp-noR1 and Exp-noR2 relative to Exp-orig were calculated (For example, the improvement rate of Exp-noR1 relative to Exp-orig was computed using the formula $\frac{|\mathrm{diff}_1|-|\mathrm{diff}_2|}{|\mathrm{diff}_1|} \times 100\%$, where diff_1 (diff_2) represents the height difference between Exp-orig (Exp-noR1) and β'_{532nm}). The fog-top height and fog-bottom height show a rise of 62% and 86%, respectively, compared to Exp-orig. In contrast, the improvement rates for Exp-noR1 are 21% and 32%, respectively. In addition, we computed the vertically integrated LWC for the three experiments. The average values obtained were 0.8 g kg^{-1} for Exp-orig, 0.9 g kg^{-1} for Exp-noR1, and 1.2 g kg^{-1} for Exp-noR2. The average value of Exp-noR2 is approximately 50% higher than that of Exp-orig, indicating the effects of dehumidifying and warming induced by the term *R*2.

Table 3. Evaluation of Exp-orig, Exp-noR1, and Exp-noR2 against the β'_{532nm} of the CALIPSO data. The percentages in parentheses denote the improvement rates relative to Exp-orig.

Average Value	β'_{532nm}	Experiments		
		Exp-orig	Exp-noR1	Exp-noR2
fog-top height (m)	132.9	145.2	142.6 (21%)	128.2 (62%)
fog-bottom height (m)	3.7	21.3	15.6 (32%)	1.2 (86%)
Average vertically integrated LWC (g kg^{-1})	/	0.8	0.9	1.2

5. Conclusions and Discussion

The entrainment zone is the region of statically stable air located in the uppermost part of the mixed layer. It acts as a bridge between the free atmosphere and the planetary boundary layer through the process of entrainment. Sea fogs over the Yellow Sea generally belong to the advection cooling type. An advection fog over the Yellow Sea typically forms within a thermal internal boundary layer, and the interior of sea fog can be regarded as a mixed layer, with the fog-top entrainment dominating the fog growing in thickness. Therefore, in the modeling of sea fog, the parameterization of fog-top entrainment is a critical issue.

The YSU PBL scheme in the WRF model includes an option ysu_topdown_pblmix, which is a parameterization for fog-top entrainment proposed by Wilson and Fovell [21] for valley radiation fog to lift ground fog upward onto the low stratus as realistically as possible. Yang and Gao [19] pointed out that sea-fog simulations can benefit from this option to improve the vertical development of sea fog and, hence, the fog area. However, when the option ysu_topdown_pblmix is activated on the WRF-based Yellow Sea fog prediction system we developed, the prediction system usually produces an unrealistic dissipation of sea fog. To explore the reason why this unrealistic dissipation is generated, we first theoretically analyzed the option and then examined it in detail through numerical simulations employing the WRF model. A widespread sea fog over the Yellow Sea was utilized as a case study, and an investigation was conducted using four experiments, including one control experiment as the baseline, and three sensitivity tests. The main conclusions are summarized as follows:

- An assessment was performed utilizing the observed facts, which included satellite visible images for identifying the fog area and fog-top horizontal distribution characteristics, as well as the $\beta'_{532\mathrm{nm}}$ signals of the CALIPSO data for contrast information for fog-top and fog-bottom heights. The option ysu_topdown_pblmix should be enabled because it essentially facilitates the vertical development of sea fog. Otherwise, the fog-top height seriously deviates from the observation and the vertical structure of LWC is far from reasonable;
- However, enabling the option ysu_topdown_pblmix produces unrealistic dissipation. Sensitivity test results, the LWC, and the θ_v budget contribution analysis show that unrealistic dissipation is directly due to the negative q_c tendency near the fog bottom resulting from evaporation in the microphysical process suppressing turbulent diffusion transport. This negative q_c tendency is a result of the entrainment–mixing feedback, where drier and warmer air is carried to the fog bottom, thereby enhancing the evaporation process. Nevertheless, the entrainment rate in the entrainment–mixing feedback is overestimated, which is attributable to the minimum threshold term in the option ysu_topdown_pblmix;
- When modeling sea fog, the option ysu_topdown_pblmix can be significantly improved by removing the redundant term $R2$, as indicated by the results of the sensitivity tests. However, this modification strategy necessitates more instances of sea fog to validate its efficacy.

Although we explained the reason why enabling the option ysu_topdown_pblmix in the WRF model causes sea fog to dissipate and provide a simple improvement method, this study is still preliminary. In the option ysu_topdown_pblmix, the key variable $\overline{(w'\theta'_v)}_h$ describing the fog-top entrainment is also added to the profile of the eddy diffusivity coefficient (i.e., K-profile), resulting in a substantial change to the original K-profile in the YSU PBL scheme when fog is present. The position of maximum LWC within the interior of sea fog may be related to this K-profile. Furthermore, the variable E in Equation (5) represents a correlation between the evaporation and fog droplets involved with the LWC at the fog top, and its coefficient α_2, derived from the results of LES [36], is still extremely uncertain. A value of 8 is currently adopted according to the LES simulation results of valley fog [21], but some studies suggest that a value of 15 is more appropriate [33], or

even a value of 60 for cloud [36]. The value of α_2 needs further exploration, especially after removing the minimum threshold amplitude 0.2. It is widely recognized that the vertical resolution of the WRF simulation is coarser compared to that of the LES. Consequently, the model's ability to reliably predict the fog-top LWC is often compromised. Additionally, the coefficient A may also be influenced by the vertical resolution. These concerns suggest that the entrainment rate w_e should be formulated as a function that depends on the vertical resolution, which is a topic worthy of further investigation in the future.

Author Contributions: Conceptualization, S.G. and L.Z.; methodology, L.Z., H.S. and S.G.; validation, S.G.; formal analysis, L.Z., H.S. and S.G.; writing—original draft preparation, L.Z.; writing—review and editing, L.Z., H.S. and S.G.; visualization, L.Z., H.S., S.L. and S.G.; project administration, S.G.; funding acquisition, S.G. All authors have read and agreed to the published version of the manuscript.

Funding: This work was funded by the National Key R&D Program of China (2022YFC3004200) and the National Natural Science Foundation of China (U2342214, 42075069).

Data Availability Statement: The eighth Himawari geostationary weather satellite (Himawari-8) is operated by the Japan Meteorological Agency (JMA) and can be accessed at: https://www.jma.go.jp (accessed on 1 March 2024). The CALIPSO (Cloud-Aerosol Lidar and Infrared Pathfinder Satellite Observation) satellite can be downloaded at https://asdc.larc.nasa.gov/data/CALIPSO (accessed on 1 March 2024). International Comprehensive Ocean-Atmosphere Data Set (ICOADS) can be downloaded at https://rda.ucar.edu/datasets/ds548.0 (accessed on 1 March 2024). The ERA5 data are archived by ECMWF (https://cds.climate.copernicus.eu/cdsapp#!/dataset/reanalysis-era5-pressure-levels (accessed on 1 March 2024)). The NEAR-GOOS SST data can be downloaded at http://ds.data.jma.go.jp/gmd/goos/data (accessed on 1 March 2024). Other data and codes for this study are available from the corresponding author upon reasonable request.

Acknowledgments: The computation for simulations and the evaluations in this study were conducted at the High-Performance Computing Center in the Ocean University of China. We appreciate the helpful discussions with Meng Tian.

Conflicts of Interest: The authors declare no conflicts of interest. The funders had no role in the design of the study; in the collection, analyses, or interpretation of data; in the writing of the manuscript; or in the decision to publish the results.

References

1. Wang, B. *Sea Fog*; China Ocean Press: Beijing, China, 1985.
2. Gultepe, I.; Tardif, R.; Michaelides, S.C.; Cermak, J.; Bott, A.; Bendix, J.; Müller, M.D.; Pagowski, M.; Hansen, B.; Ellrod, G.; et al. Fog Research: A Review of Past Achievements and Future Perspectives. *Pure Appl. Geophys.* **2007**, *164*, 1121–1159. [CrossRef]
3. Gao, S.; Lin, H.; Shen, B.; Fu, G. A heavy sea fog event over the Yellow Sea in March 2005: Analysis and numerical modeling. *Adv. Atmos. Sci.* **2007**, *24*, 65–81. [CrossRef]
4. Zhang, S.-P.; Xie, S.-P.; Liu, Q.-Y.; Yang, Y.-Q.; Wang, X.G.; Ren, Z.P. Seasonal Variations of Yellow Sea Fog: Observations and Mechanisms. *J. Clim.* **2009**, *22*, 6758–6772. [CrossRef]
5. Jin, G.; Gao, S.; Shi, H.; Lu, X.; Yang, Y.; Zheng, Q. Impacts of Sea–Land Breeze Circulation on the Formation and Development of Coastal Sea Fog along the Shandong Peninsula: A Case Study. *Atmosphere* **2022**, *13*, 165. [CrossRef]
6. Jacovides, C.P.; Varotsos, C.A.; Kaltsounides, N.A.; Petrakis, M.; Lalas, D.P. Atmospheric turbidity parameters in the highly polluted site of Athens basin. *Renew. Energy* **1994**, *4*, 465–470. [CrossRef]
7. Nicholls, S. The dynamics of stratocumulus: Aircraft observations and comparisons with a mixed layer model. *Q. J. R. Meteorol. Soc.* **1984**, *110*, 783–820. [CrossRef]
8. Findlater, J.; Roach, W.T.; McHugh, B.C. The haar of north-east Scotland. *Q. J. R. Meteorol. Soc.* **1989**, *115*, 581–608. [CrossRef]
9. Gao, S.; Qi, Y.; Zhang, S.; Fu, G. Initial Conditions Improvement of Sea Fog Numerical Modeling over the Yellow Sea by Using Cycling 3DVAR Part I: WRF Numerical Experiments. *J. Ocean Univ. China* **2010**, *40*, 1–9.
10. Wang, Y.; Gao, S.; Fu, G.; Sun, J.; Zhang, S. Assimilating MTSAT-Derived Humidity in Nowcasting Sea Fog over the Yellow Sea. *Weather Forecast.* **2014**, *29*, 205–225. [CrossRef]
11. Gao, X.; Gao, S.; Li, Z.; Wang, Y. A revised method with a temperature constraint for assimilating satellite-derived humidity in forecasting sea fog over the Yellow Sea. *Front. Earth Sci.* **2023**, *10*, 992246. [CrossRef]
12. Skamarock, W.C.; Klemp, J.B.; Dudhia, J.; Gill, D.O.; Barker, D.; Wang, W.; Powers, J.G. A Description of the Advanced Research WRF Version 3. 2008, Volume 27, pp. 3–27. Available online: http://opensky.ucar.edu/islandora/object/technotes:500 (accessed on 1 March 2024).

13. Skamarock, W.C.; Klemp, J.B.; Dudhia, J.; Gill, D.O.; Liu, Z.; Berner, J.; Wang, W.; Powers, G.; Duda, G.; Barker, D.M.; et al. A Description of the Advanced Research WRF Model Version 4.3. 2021. Available online: https://opensky.ucar.edu/islandora/object/technotes:588 (accessed on 1 March 2024).
14. Hong, S.-Y.; Noh, Y.; Dudhia, J. A new vertical diffusion package with an explicit treatment of entrainment processes. *Mon. Weather Rev.* **2006**, *134*, 2318–2341. [CrossRef]
15. Lin, Y.-L.; Farley, R.D.; Orville, H.D. Bulk Parameterization of the Snow Field in a Cloud Model. *J. Appl. Meteorol. Climatol.* **1983**, *22*, 1065–1092. [CrossRef]
16. Chen, S.H.; Sun, W.Y. A one-dimensional time dependent cloud model. *J. Meteorol. Soc. Jpn.* **2002**, *80*, 99–118. [CrossRef]
17. Lu, X.; Gao, S.; Rao, L.; Wang, Y. Sensitivity Study of WRF Parameterization Schemes for the Spring Sea Fog in the Yellow Sea. *J. Appl. Meteorolgical Sci.* **2014**, *25*, 312–320.
18. Yang, Y.; Hu, X.-M.; Gao, S.; Wang, Y. Sensitivity of WRF simulations with the YSU PBL scheme to the lowest model level height for a sea fog event over the Yellow Sea. *Atmos. Res.* **2019**, *215*, 253–267. [CrossRef]
19. Yang, Y.; Gao, S. The Impact of Turbulent Diffusion Driven by Fog-Top Cooling on Sea Fog Development. *J. Geophys. Res. Atmos.* **2020**, *125*, e2019JD031562. [CrossRef]
20. Tokinaga, H.; Xie, S.P. Ocean tidal cooling effect on summer sea fog over the Okhotsk Sea. *J. Geophys. Res.* **2009**, *114*, D14102. [CrossRef]
21. Wilson, T.H.; Fovell, R.G. Modeling the Evolution and Life Cycle of Radiative Cold Pools and Fog. *Weather Forecast.* **2018**, *33*, 203–220. [CrossRef]
22. Pithani, P.; Ghude, S.D.; Prabhakaran, T.; Karipot, A.; Hazra, A.; Kulkarni, R.; Chowdhuri, S.; Resmi, E.A.; Konwar, M.; Murugavel, P.; et al. WRF model sensitivity to choice of PBL and microphysics parameterization for an advection fog event at Barkachha, rural site in the Indo-Gangetic basin, India. *Theor. Appl. Climatol.* **2019**, *136*, 1099–1113. [CrossRef]
23. Stull, R.B. *An Introduction to Boundary Layer Meteorology*; Kluwer Academic Publishers: Dordrecht, The Netherlands, 1988.
24. Lewis, J.M.; Koračin, D.; Redmond, K.T. Sea fog research in the United Kingdom and United States—A historical essay including outlook. *Bull. Am. Meteorol. Soc.* **2004**, *85*, 395–408. [CrossRef]
25. Tardif, R.; Rasmussen, R.M. Event-Based Climatology and Typology of Fog in the New York City Region. *J. Appl. Meteorol. Climatol.* **2007**, *46*, 1141–1168. [CrossRef]
26. Yang, Y.; Gao, S. Sensitivity study of vertical resolution in WRF numerical simulation for sea fog over the Yellow Sea. *Acta Meteorol. Sin.* **2016**, *74*, 974–988.
27. Brown, R.; Roach, W.T. The physics of radiation fog: II—A numerical study. *Q. J. R. Meteorol. Soc.* **1976**, *102*, 335–354. [CrossRef]
28. Kim, C.K.; Yum, S.S. A Numerical Study of Sea-Fog Formation over Cold Sea Surface Using a One-Dimensional Turbulence Model Coupled with the Weather Research and Forecasting Model. *Bound.-Layer Meteorol.* **2012**, *143*, 481–505. [CrossRef]
29. Koračin, D.; Dorman, C.E.; Lewis, J.M.; Hudson, J.G.; Wilcox, E.M.; Torregrosa, A. Marine fog: A review. *Atmos. Res.* **2014**, *143*, 142–175. [CrossRef]
30. Yang, L.; Liu, J.-W.; Xie, S.-P.; Shen, S.S.P. Transition from Fog to Stratus over the Northwest Pacific Ocean: Large-Eddy Simulation. *Mon. Weather Rev.* **2021**, *149*, 2913–2925. [CrossRef]
31. Tian, M.; Wu, B.; Liao, Y.; Yang, J.; Liu, H. The Influence of Turbulent Diffusion Driven by Fog-Top Radiative Cooling on Heavy Fog in North China Plain. *Chin. J. Atmos. Sci.* **2023**, *in press*. [CrossRef]
32. Tennekes, H. A Model for the Dynamics of the Inversion Above a Convective Boundary Layer. *J. Atmos. Sci.* **1973**, *30*, 558–567. [CrossRef]
33. Bretherton, C.S.; Blossey, P.N.; Uchida, J. Cloud droplet sedimentation, entrainment efficiency, and subtropical stratocumulus albedo. *Geophys. Res. Lett.* **2007**, *34*, L03813. [CrossRef]
34. Driedonks, A.G.M. Models and observations of the growth of the atmospheric boundary layer. *Bound.-Layer Meteorol.* **1982**, *23*, 283–306. [CrossRef]
35. Moeng, C.H.; Sullivan, P.P. A Comparison of Shear- and Buoyancy-Driven Planetary Boundary Layer Flows. *J. Atmos. Sci.* **1994**, *51*, 999–1022. [CrossRef]
36. Nicholls, S.; Turton, J.D. An observational study of the structure of stratiform cloud sheets: Part II Entrainment. *Q. J. R. Meteorol. Soc.* **1986**, *112*, 461–480. [CrossRef]
37. Bretherton, C.S.; Wyant, M.C. Moisture Transport, Lower-Tropospheric Stability, and Decoupling of Cloud-Topped Boundary Layers. *J. Atmos. Sci.* **1997**, *54*, 148–167. [CrossRef]
38. Fu, G.; Li, P.; Crompton, J.G.; Guo, J.; Gao, S.; Zhang, S. An observational and modeling study of a sea fog event over the Yellow Sea on 1 August 2003. *Meteorol. Atmos. Phys.* **2010**, *107*, 149–159. [CrossRef]
39. Schwenkel, J.; Maronga, B. Large-eddy simulation of radiation fog with comprehensive two-moment bulk microphysics: Impact of different aerosol activation and condensation parameterizations. *Atmos. Chem. Phys.* **2019**, *19*, 7165–7181. [CrossRef]
40. Yan, S.; Zhu, B.; Huang, Y.; Zhu, J.; Kang, H.; Lu, C.; Zhu, T. To what extents do urbanization and air pollution affect fog? *Atmos. Chem. Phys.* **2020**, *20*, 5559–5572. [CrossRef]
41. Yan, S.; Wang, H.; Liu, X.; Zu, F.; Liu, D. Effect of the boundary layer low-level jet on fast fog spatial propagation. *Atmos. Chem. Phys.* **2023**, *23*, 13987–14002. [CrossRef]

42. Bessho, K.; Date, K.; Hayashi, M.; Ikeda, A.; Imai, T.; Inoue, H.; Kumagai, Y.; Miyakawa, T.; Murata, H.; Ohno, T. An Introduction to Himawari-8/9—Japan's New-Generation Geostationary Meteorological Satellites. *J. Meteorol. Soc. Japan. Ser. II* **2016**, *94*, 151–183. [CrossRef]
43. Powell, K.A.; Hostetler, C.A.; Vaughan, M.A.; Lee, K.-P.; Trepte, C.R.; Rogers, R.R.; Winker, D.M.; Liu, Z.; Kuehn, R.E.; Hunt, W.H. CALIPSO Lidar Calibration Algorithms. Part I: Nighttime 532-nm Parallel Channel and 532-nm Perpendicular Channel. *J. Atmos. Ocean. Technol.* **2009**, *26*, 2015–2033. [CrossRef]
44. Wu, D.; Lu, B.; Zhang, T.; Yan, F. A method of detecting sea fogs using CALIOP data and its application to improve MODIS-based sea fog detection. *J. Quant. Spectrosc. Radiat. Transf.* **2015**, *153*, 88–94. [CrossRef]
45. Hersbach, H.; Bell, B.; Berrisford, P.; Hirahara, S.; Horányi, A.; Muñoz-Sabater, J.; Nicolas, J.; Peubey, C.; Radu, R.; Schepers, D. The ERA5 global reanalysis. *Q. J. R. Meteorol. Soc.* **2020**, *146*, 1999–2049. [CrossRef]
46. Zhang, J.; Zhang, S.; Wu, X.; Liu, Y.; Liu, J. The Research on Yellow Sea Sea Fog Based on MODIS Data:Sea Fog Properties Retrieval and Spatial-Temporal Distribution. *Period. Ocean Univ. China* **2009**, *39* (S1), 311–318.
47. Huang, B.; Xu, J.; Shi, D.; Liu, L. Deformation Feature of a Continuous Sea Fog Process over the Yellow Sea and Bohai Sea and Its Genesis Analysis. *Meteorol. Mon.* **2018**, *44*, 1342–1351.
48. Liu, L.; Liu, L.; Huang, B. Observation and numerical simulation on a sea fog event under the background of an extratropical cyclone entering sea. *Chin. J. Atmos. Sci.* **2023**, *in press*.
49. Jiménez, P.A.; Dudhia, J.; González-Rouco, J.F.; Navarro, J.; Montávez, J.P.; García-Bustamante, E. A Revised Scheme for the WRF Surface Layer Formulation. *Mon. Weather Rev.* **2012**, *140*, 898–918. [CrossRef]
50. Iacono, M.J.; Delamere, J.S.; Mlawer, E.J.; Shephard, M.W.; Clough, S.A.; Collins, W.D. Radiative forcing by long-lived greenhouse gases: Calculations with the AER radiative transfer models. *J. Geophys. Res.-Atmos.* **2008**, *113*, D13103. [CrossRef]
51. Kain, J.S. The Kain–Fritsch Convective Parameterization: An Update. *J. Appl. Meteorol.* **2004**, *43*, 170–181. [CrossRef]
52. Tewari, M.; Chen, F.; Wang, W.; Dudhia, J.; Lemone, M.A.; Mitchell, K.E.; Ek, M.B.; Gayno, G.; Węgiel, W.; Cuenca, R.H. Implementation and verification of the unified Noah land-surface model in the WRF model [presentation]. In Proceedings of the 20th Conference on Weather Analysis and Forecasting/16th Conference on Numerical Weather Prediction, Seattle, WA, USA, 12–16 January 2004.
53. Bergot, T.; Terradellas, E.; Cuxart, J.; Mira, A.; Liechti, O.; Mueller, M.; Nielsen, N.W. Intercomparison of Single-Column Numerical Models for the Prediction of Radiation Fog. *J. Appl. Meteorol. Climatol.* **2007**, *46*, 504–521. [CrossRef]
54. Zhou, B.; Ferrier, B.S. Asymptotic analysis of equilibrium in radiation fog. *J. Appl. Meteorol. Climatol.* **2008**, *47*, 1704–1722. [CrossRef]
55. Gao, X.; Gao, S.; Yang, Y. A Comparison between 3DVAR and EnKF for Data Assimilation Effects on the Yellow Sea Fog Forecast. *Atmosphere* **2018**, *9*, 346. [CrossRef]
56. Zhou, B.; Du, J. Fog Prediction from a Multimodel Mesoscale Ensemble Prediction System. *Weather Forecast.* **2010**, *25*, 303–322. [CrossRef]
57. Stoelinga, M.T.; Warner, T.T. Nonhydrostatic, Mesobeta-Scale Model Simulations of Cloud Ceiling and Visibility for an East Coast Winter Precipitation Event. *J. Appl. Meteorol.* **1999**, *38*, 385–404. [CrossRef]
58. Yang, L.; Liu, J.-W.; Ren, Z.-P.; Xie, S.-P.; Zhang, S.-P.; Gao, S.-H. Atmospheric Conditions for Advection-Radiation Fog Over the Western Yellow Sea. *J. Geophys. Res.-Atmos.* **2018**, *123*, 5455–5468. [CrossRef]